

Real-space and plane-wave combination for electronic structure calculation of two-dimensional materials

V. Nam Do,^{a*} and H. Anh Le,^b V. Thieu Vu^c

^a*Advanced Institute for Science and Technology (AIST),*

^b*International Institute for Computational Science and Engineering (ICSE),*

^c*School of Information and Communication Technology (SoICT),*

Hanoi University of Science and Technology (HUST), 01 Dai Co Viet road, Hanoi, Vietnam

(Dated: today)

We propose an approach to combining the plane-wave method and the real-space treatment to characterise the periodic variation and the decay of wave functions in the material plane and from the material surfaces. The proposed approach is natural for 2D material systems, and thus may circumvent some intrinsic limitations involving the artificial replication of material layer in traditional supercell methods. In particular, we show that the proposed method is easy to implement and, especially, computationally effective since low-cost computational algorithms, such as iterative and recursive techniques, can be used to treat matrices with block tridiagonal structure. Using the proposed approach we show first-principles evidences to supplement the current knowledge of some fundamental issues in bilayer graphene systems, including the coupling between the two graphene layers, the preservation of the σ -band of monolayer graphene in the electronic structure of the bilayer system, and the difference between the low-energy band structure of the AA- and AB-stacked configurations.

I. INTRODUCTION

Since the successful isolation of graphene in 2004,¹ a number of other two-dimensional materials have been discovered and have been attracting an intense consideration in a wide range of research fields. It has been shown that these materials offer the flexibility to be assembled in various configurations to form van der Waals heterostructures.² With unprecedented properties, such systems are expected to lead to major technological advances.³

For any crystalline material, the electronic structure is the primary information needed for the analysis of its basic properties, including the transport, optic, magnetic properties, etc.. From the computational point of view, the electronic structure of a material is usually calculated using methods, namely the 3D ones, which are based on the periodicity of the crystalline lattice along all three spatial dimensions. The 2D material systems, however, are naturally assumed to be periodic in two dimensions and finite along the third one. To use the 3D approach one needs to construct an artificial 3D system from the given 2D one by defining a box with the bottom chosen as the unit cell of the 2D lattice and a sufficiently large height along the perpendicular direction. This box, called supercell, is then replicated not only along the material plane, but also along the perpendicular direction to form a 3D periodic atomic lattice. This approach, though feasible for calculation, is flawed by several conceptual problems involving the interaction between the material replicas. The inter-replica interaction stems from the long-range nature of the Coulomb potential which cannot be screened at sufficient large distance from the plane of the material layer due to the quasi-two dimensional character of the electronic charge distribution.⁴⁻⁶ The common technique consists in choosing a large dis-

tance between the replicas with the hope of ignoring the inter-replica interaction. However, because of the failure of screening, the Coulomb interaction between artificial replica cannot be totally ignored and thus may cause spurious results as recently highlighted by Nazarov in the dynamical response properties of graphene.⁷ Other computational techniques have been additionally introduced to treat this issue. The most rough technique is to truncate the Coulomb interaction beyond a certain cutoff distance in the z direction.⁸ Another more complicated solution is to calculate the mean field created by the replicas and subtract it from the field that acts on the electrons in the material layer.⁹

In addition to the lost of the nature of 2D systems, the 3D approach is extremely costly from the computational point of view. Since periodic functions, for instance, plane waves, are used to represent the electron states, we have to determine eigen-values and eigen-vectors of very large matrices which have a full square structure. For 2D systems, remarkably, the matrix dimension is not fixed by only a cutoff kinetic energy, E_{cutoff} , but also by the inter-replica spacing d . For a given value of E_{cutoff} the number of plane waves rapidly increases when increasing the inter-replica spacing due to the contribution of the reciprocal vectors (whose length is multiple of $2\pi/d$) along the z -direction.

It is common that an efficient treatment for the Schrodinger-like equation should lie on the choice of an appropriate basis to represent solutions. For the electronic structure of 2D materials, it was suggested that a relevant basis should be a set of functions which are periodic in the (x,y) plane and atomic-like in the z direction.^{10,11} Along this line, Trevisanutto and Vignale proposed to use a set of functions called Natural Atom-centered Orbitals which are numerically generated by, for instance, the FHI-AIMS (Fritz-Haber ab-initio molecular

simulation) code.^{12,13} To treat the electronic structure of 2D materials with a thickness of several atomic layers we propose in this paper the combination of the plane wave method to represent the periodic variation of the electron wave functions in the material plane and the real-space treatment based on the finite differential method to describe the decay of the wave functions from the material surfaces. We show that the proposed approach leads to working with matrices having the block tridiagonal structure. As a result, low-cost computational algorithms, such as iterative and recursive techniques, can be efficiently implemented.^{14,15} Beyond that, a nonuniform meshing scheme can be used to reduce the number of blocks in involved matrices, thus, accelerating the computation.

To demonstrate the natural applicability of the proposed approach for 2D systems the thickness of which is of several atomic layers we use graphene in the conventional configurations of monolayer and bilayer as material platforms to compare the results obtained from the 2D and 3D approaches. Our electronic calculation is based on the empirical pseudopotential method using the potential calibrated by Kurokawa *et al.* for carbon.¹⁷ Based on the obtained results for the lattice potential and the electronic structure we revisit the issues of the preservation of the σ -bands of the monolayer in the spectrum of the bilayer system, the qualitative difference in the low-energy excited spectrum of the AA- and AB-stacking bilayer configurations, and particularly the coupling of the two graphene layers.

This article is organised as follows. In the next section, Sec. II, we present the formulation of the proposed 2D approach. The energy band structure as well as the wave functions for some specific electronic states of monolayer and AB- and AA-stacking bilayer graphene are presented

in Sec. III. Finally, section IV is for the conclusion.

II. METHOD AND FORMULATION

Let $\mathbf{r} = (x, y)$ be the coordinate vector in the xy -plane in which the 2D material layer lies in. The crystalline lattice potential is thus written in the form $V(\mathbf{r}, z)$ which is periodic in the material plane and naturally decays from the material surfaces, i.e., $V(\mathbf{r} + \mathbf{R}, z) = V(\mathbf{r}, z)$ where \mathbf{R} is a lattice vector, and $V(\mathbf{r}, z \rightarrow \pm\infty) = 0$. The determination of the electronic structure of a material system is theoretically achieved by solving the Schrodinger-like equation:

$$\left[-\frac{\hbar^2}{2m_0} (\nabla_{\mathbf{r}}^2 + \partial_z^2) + V(\mathbf{r}, z) \right] \psi(\mathbf{r}, z) = E\psi(\mathbf{r}, z), \quad (1)$$

where m_0 is the mass of bare electron, \hbar is the reduced Planck constant, and $E, \psi(\mathbf{r}, z)$ are the eigen-values and eigen-functions, which have to be determined. Taking into account the periodicity of the crystal lattice all possible solutions of the Schrodinger-like equation can be written in the form:

$$\psi_{\mathbf{k}}(\mathbf{r}, z) = \frac{1}{\sqrt{S}} \sum_{\mathbf{g}} e^{i(\mathbf{k}+\mathbf{g})\mathbf{r}} a_{\mathbf{k},\mathbf{g}}(z), \quad (2)$$

where \mathbf{k} is a real two-dimensional vector of the first Brillouin zone, $a_{\mathbf{k},\mathbf{g}}(z)$ are the unknown coefficients defined for each two-dimensional vector \mathbf{g} , and S is the area of the whole surface of the material layer. The summation in the above equation is over all the possible reciprocal lattice vectors \mathbf{g} which satisfy the condition $\mathbf{g} \cdot \mathbf{R} = 2\pi n$ where n is an integer number. Using expression (2), Eq. (1) is rewritten in the following form:

$$\frac{1}{\sqrt{S}} \sum_{\mathbf{g}} e^{i(\mathbf{k}+\mathbf{g})\mathbf{r}} \left\{ -\frac{\hbar^2}{2m} \partial_z^2 a_{\mathbf{k},\mathbf{g}}(z) + \left[\frac{\hbar^2}{2m} (\mathbf{k} + \mathbf{g})^2 + V(\mathbf{r}, z) \right] a_{\mathbf{k},\mathbf{g}}(z) \right\} = \frac{1}{\sqrt{S}} \sum_{\mathbf{g}} e^{i(\mathbf{k}+\mathbf{g})\mathbf{r}} E_{\mathbf{k}} a_{\mathbf{k},\mathbf{g}}(z). \quad (3)$$

To deduce the equations for the unknown coefficients $a_{\mathbf{k},\mathbf{g}}(z)$ we multiply both sides of the above equation by $e^{-i(\mathbf{k}+\mathbf{g}')\mathbf{r}}/\sqrt{S}$ and then integrate over \mathbf{r} in the whole (x, y) plane, it yields:

$$-\frac{\hbar^2}{2m} \partial_z^2 a_{\mathbf{k},\mathbf{g}'}(z) + \frac{\hbar^2}{2m} (\mathbf{k} + \mathbf{g}')^2 a_{\mathbf{k},\mathbf{g}'}(z) + \sum_{\mathbf{g}} V(\mathbf{g}' - \mathbf{g}, z) a_{\mathbf{k},\mathbf{g}}(z) = E_{\mathbf{k}} a_{\mathbf{k},\mathbf{g}'}(z), \quad (4)$$

wherein we have set

$$V(\mathbf{g}' - \mathbf{g}, z) = \frac{1}{S} \int d\mathbf{r} V(\mathbf{r}, z) e^{-i(\mathbf{g}' - \mathbf{g})\mathbf{r}}. \quad (5)$$

The expression of $V(\mathbf{g}, z)$ defined by Eq. (5) is nothing

but the Fourier transform of the lattice potential in the (x, y) plane. Equation (4) is actually a representative for a set of dependent linear equations written for all unknown coefficients $a_{\mathbf{k},\mathbf{g}}(z)$ whose variation versus z is characterised by the second-order derivative term. In the case where $V(\mathbf{g}' - \mathbf{g}, z)$ is periodic with respect to z we can expand $a_{\mathbf{k},\mathbf{g}}(z)$ via a Fourier series and thus Eq. (4) becomes identical to the central equation of the conventional three-dimensional plane wave method.

Assuming that the material is of few atomic layers, it is natural to describe the decay of the electron wave functions from the material surfaces by using the finite differential method to specify the derivative term. By setting $t_z = \hbar^2/2m\delta_z^2$ in which δ_z is the meshing spacing

of the variable z , i.e., $\delta_z = z_i - z_{i-1}$, we rewrite Eq. (4)

in the discrete form:

$$\sum_{i,\mathbf{g}} \left[-t_z \delta_{\mathbf{g},\mathbf{g}'} \delta_{i,j-1} + \left[\left(2t_z + \frac{\hbar^2}{2m} (\mathbf{k} + \mathbf{g}')^2 - E_{\mathbf{k}} \right) \delta_{\mathbf{g},\mathbf{g}'} + V_i(\mathbf{g}' - \mathbf{g}) \right] \delta_{i,j} - t_z \delta_{\mathbf{g},\mathbf{g}'} \delta_{i,j+1} \right] a_{\mathbf{k},\mathbf{g}}^i = 0, \quad (6)$$

where $\delta_{\mathbf{g},\mathbf{g}'}$ and $\delta_{i,j}$ denote the Kronecker symbols for the corresponding indices, and $a_{\mathbf{k},\mathbf{g}}(z_i)$ is shortened by $a_{\mathbf{k},\mathbf{g}}^i$. So far we have not yet limited the range of z , i.e., $-\infty < z < +\infty$. However, in order to numerically solve a large system of equations represented by Eq. (6) we need to limit z in the range $[z_1, z_{N_z}]$ (N_z is the number of meshing points $\{z_i\}$) that contains the material thickness in the centre. By taking into account the fact that the electron wave functions must decay at a sufficiently large distance from the material surfaces we impose the Neumann condition on all $a_{\mathbf{k},\mathbf{g}}(z)$ at the two

ends. Specifically we impose $\partial_z a_{\mathbf{k},\mathbf{g}}(z) = 0$ at $z = z_1$ and $z = z_{N_z}$. Numerically, these conditions are equivalent to $a_{\mathbf{k},\mathbf{g}}(z_0) = a_{\mathbf{k},\mathbf{g}}(z_1)$ and $a_{\mathbf{k},\mathbf{g}}(z_{N_z+1}) = a_{\mathbf{k},\mathbf{g}}(z_{N_z})$. Using the plane wave and finite differential representations we transform Eq. (1) from its analytic form to a set of linear uniform equations for a set of unknown coefficients $\{a_{\mathbf{k},\mathbf{g}}^i\}$. Numerically, it is convenient to define a column vector $a_{\mathbf{k}}$ whose the components $\{a_{\mathbf{k},\mathbf{g}}^i\}$ are organised in the order

$$a_{\mathbf{k}} = (\dots, [\dots, a_{\mathbf{k},\mathbf{g}_{j-1}}^{i-1}, a_{\mathbf{k},\mathbf{g}_j}^{i-1}, a_{\mathbf{k},\mathbf{g}_{j+1}}^{i-1}, \dots], [\dots, a_{\mathbf{k},\mathbf{g}_{j-1}}^i, a_{\mathbf{k},\mathbf{g}_j}^i, a_{\mathbf{k},\mathbf{g}_{j+1}}^i, \dots], \dots)^T. \quad (7)$$

The equations given by (6) are now rewritten into the familiar eigenvalue equation $H_{\mathbf{k}} a_{\mathbf{k}} = E_{\mathbf{k}} a_{\mathbf{k}}$ wherein $H_{\mathbf{k}}$ is a hermitian matrix with the block tridiagonal structure. It is useful to elaborate on this matrix. All diagonal blocks $[H_{\mathbf{k}}]_{n,n}$ are the full square matrices due to the presence of the potential $V_i(\mathbf{g}' - \mathbf{g})$. The diagonal elements of these blocks are simply given by $2t_z + \hbar^2(\mathbf{k} + \mathbf{g}')^2/2m_0 + V_i(0)$, except the first and last elements are given by $t_z + \hbar^2(\mathbf{k} + \mathbf{g}')^2/2m_0 + V_i(0)$ due to the inclusion of the boundary conditions. The super- and sub-diagonal blocks are simply the diagonal matrices taking the same form of $[H_{\mathbf{k}}]_{n,n\pm 1} = -t_z[I]$, where $[I]$ denotes the identity matrix. The size of each block is determined by the number of the \mathbf{g} -vectors, $N_{\mathbf{g}}$, i.e., the

plane wave numbers used to represent the wave function (2), while the number of matrix blocks is defined by the number of meshing points z_i in the interval $[z_1, z_{N_z}]$. In the next section we will show that with the block tridiagonal structure the secular equation defined by the matrix $H_{\mathbf{k}}$ is efficiently solved using available solvers based on the direct or iterative methods. The recursive technique is also useful for the computation of the spectrum function associated with $H_{\mathbf{k}}$.

Last but not least, in order to complete the definition of all terms in Eq. (6) one should discuss about the way to determine the values of $V_i(\mathbf{g}) = V(\mathbf{g}, z_i)$. In our study we use the empirical pseudopotential approach and thus specify the lattice potential as follows:

$$V(\mathbf{g}, z) = \frac{V_{\text{atom}}}{S_{\text{cell}}} \sum_{i=1}^{N_a} W_i e^{-i\mathbf{g}\mathbf{d}_i} \int_{-\infty}^{+\infty} \frac{dq_z}{2\pi} v_i(\mathbf{g}, q_z) e^{iq_z(z-d_i^z)}, \quad (8)$$

where N_a is the number of atoms whose (x, y) -coordinates are restricted in the 2D unit cell of the area S_{cell} and the z -coordinate is given by d_i^z , $v_i(\mathbf{g}, q_z)$ is the Fourier transform of the pseudopotential of atom i which is normalised by the atomic volume in the bulk unit cell V_{atom} , and W_i is the parameter defining the presence of one atom at the position (\mathbf{d}_i, d_i^z) . In practice, the atomic pseudopotential $v_i(\mathbf{q})$ can be found by a fitting procedure or by the semi-empirical manner as described in

Ref. [16]. Usually, one assumes the spherical symmetry of the pseudopotential so the dependence of v_i on \mathbf{q} is simply dependent on the modulus of this vector, i.e., $v_i(\mathbf{q}) = v_i(q)$. For our method proposed here it is convenient to write $v_i(\mathbf{q}, q_z) = v_i(\sqrt{q^2 + q_z^2})$. Given an expression, or a numeric table, for $v_i(q)$ the integral in equation (8) is numerically calculated to obtain $V(\mathbf{g}, z)$, for each value of \mathbf{g} . These values are obtained independently of \mathbf{k} so that they are just calculated in one shot and then

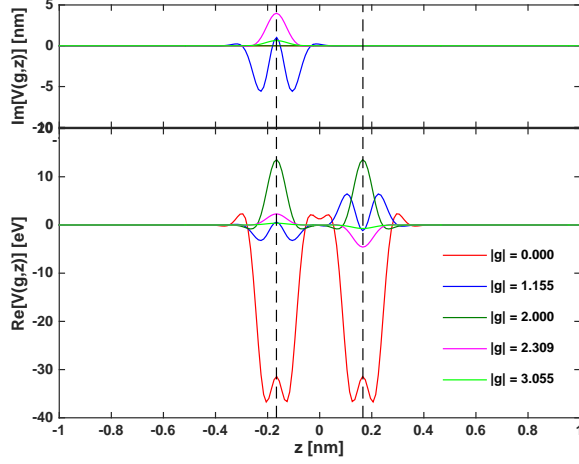


FIG. 1. Variation of the potential $V(\mathbf{g}, z)$ versus z in AB-stacked bilayer graphene, calculated for several values of the \mathbf{g} -vector (given in the unit of $2\pi/a_0$, where $a_0 = 2.46 \text{ \AA}$ is the graphene lattice constant); the imaginary/real part is shown in the top/bottom panel. The two black vertical dashed lines denote the position of the two graphene layers.

$$V(\mathbf{g}, z) = \frac{V_{\text{atom}}}{S_{\text{cell}}} \sum_{\ell=1}^{N_{\text{layer}}} \left[\sum_{i=1}^{N_a^\ell} W_i^\ell e^{-i\mathbf{g}\mathbf{d}_i^\ell} \right] \int_{-\infty}^{+\infty} \frac{dq_z}{2\pi} v_\ell(\mathbf{g}, q_z) e^{iq_z(z-z^\ell)}. \quad (9)$$

In the above equation $v_\ell(\mathbf{g}, q_z)$ is the Fourier transform of the atomic pseudopotential of a representative atom in the layer ℓ perpendicular to the z -direction at the position z^ℓ , \mathbf{d}_i^ℓ are the vector denoting the specific position of the atom i in the layer ℓ , N_a^ℓ is the number of atoms lying in the layer ℓ limited in the 2D unit cell.

To perform the electronic calculation for mono-layer and bilayer graphene, the two typical pure two-dimensional materials, we used the semi-empirical pseudopotential approach to construct the potential $V(\mathbf{g}, z)$. Specifically, we used the pseudopotential calibrated by Kurokawa *et al.* for carbon in the diamond lattice.¹⁷ For the convenience we rewrite the original expression in the following form:

$$v(q) = a_1 \frac{a_3 q^2 - a_2}{1 + a_4 \exp(a_3 q^2 - a_2)}, \quad (10)$$

in which the value of four parameters is recalculated and given (in the atomic units) by $a_1 = 1.781, a_2 = 1.424, a_3 = 0.354, a_4 = 10.612$. Note that the value of $v(q)$ given by Eq. (9) is normalised by the atomic volume of carbon in the diamond lattice, that is why V_{atom} explicitly appears in Eq. (9). This empirical pseudopotential was demonstrated by Fischetti to work well for carbon in graphene and graphene nanoribbons.¹⁸ Using Eqs. (10) and (9) we calculate and present $V(\mathbf{g}, z)$ in Figure 1 for the case of AB-stacking bilayer graphene. In

stored in a common array variable invoked during the construction procedure for the matrix $H_{\mathbf{k}}$.

III. DISCUSSIONS

The implementation of the formulation presented in the previous section is straightforward. However, one must pay attention on Eq. (8) to calculate the potential $V(\mathbf{g}, z)$. Accordingly, one needs to perform N_a integrands over q_z wherein N_a is the number of atoms in the unit cell. The calculation becomes expensive if N_a is large. However, this computational task can be significantly reduced by noting that in a crystalline lattice atoms of the same kind are usually arranged in the same planes. Accordingly, we distinguish such atomic planes by assigning for each the label ℓ , and thus in the plane ℓ all atoms are in the same kind of ℓ . Let N_{layer} be the number of such planes, this notice helps to reduce N_a integrands over q_z to just a few, equal to N_{layer} . The expression for $V(\mathbf{g}, z)$ is thus rewritten as follows:

general, for different values of \mathbf{g} we observe the asymmetric behaviour of $V(\mathbf{g}, z)$ versus z (see the blue curve), but it is not the case for AA-stacking bilayer graphene (not shown). As shown later on, this explains the qualitative difference between the electronic structures of AA- and AB-stacking bilayer graphene. Anyways, regarding the asymptotic behaviour of the potential we safely limit the range of z in the interval $[-z_0 - w/2, w/2 + z_0]$, where w is the thickness of the material layer ($w = 0$ in the case of mono-layer graphene and $w = 0.332 \text{ nm}$ in the case of bilayer graphene) and z_0 is chosen to be 0.5 nm .

Let us now specify the parameters which govern the dynamical matrix size. The first one, in both 3D and 2D approaches, is the so-called cutoff energy E_{cutoff} which defines the number $N_{\mathbf{g}}$ of \mathbf{g} -vectors used to represent the electron wave functions. In the 3D approach the dimension N_{size} of the matrix $H_{\mathbf{k}}$ is uniquely defined by $N_{\mathbf{g}}$ which is proportional to $d \times S_{\text{cell}} \times E_{\text{cutoff}}^{3/2}$, where d is the inter-replica distance (the second parameter). For the 2D approach, the size of $H_{\mathbf{k}}$ is not only determined by the number of two-dimensional \mathbf{g} -vectors, but also by the number N_z of meshing points in a chosen z -interval, i.e., $N_{\text{size}} = N_z N_{\mathbf{g}}$. If choosing the z -interval width $(2z_0 + w)$ equal to d then $N_{\text{size}} \propto d \times S_{\text{cell}} \times E_{\text{cutoff}}/\delta$, where δ (the third parameter) is the mesh spacing of z -points. Accordingly, we see that the ratio of the matrix size in the 3D approach and that in 2D one is proportional

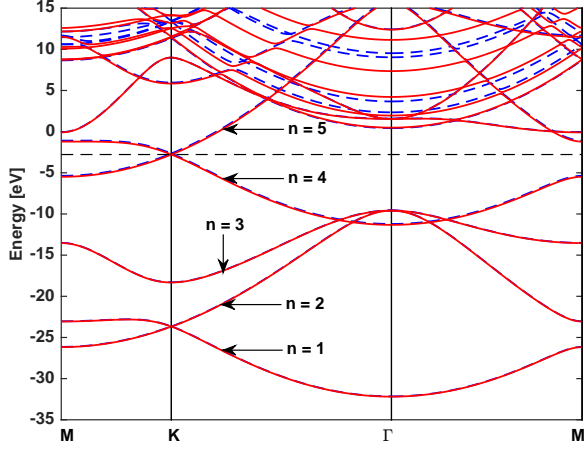


FIG. 2. Electronic band structure of monolayer graphene calculated by two approaches: the blue dashed lines are resulted from the 3D approach, and the red solid lines are from the 2D approach. The bands are not shifted so the Fermi energy is determined to be $E_F \approx -2.695$ eV as illustrated by the black dashed line.

to $(E_{\text{cutoff}}/E_\delta)^{1/2}$ with $E_\delta = \hbar^2/(2m_0\delta^2)$ characterising the hopping energy between two nearest z -points. If the mesh spacing is chosen to be $\delta_z \# 0.1 \text{ \AA}$ and $E_{\text{cutoff}} \# 30$ Ryd for carbon systems, the size of matrices in the 3D approach is quite similar to that in the 2D approach. We see that the matrix size is determined by two parameters (d and E_{cutoff}) in the 3D approach, but by three parameters (z_0, δ and E_{cutoff}) in the 2D approach. The 2D approach therefore provides a possibility to flexibly control the size of the matrix $H_{\mathbf{k}}$ (for instance, using the nonuniform meshing scheme), and thus improve the computational performance. Indeed, we verified that in order to obtain good results for the band structure of monolayer graphene using the 3D approach E_{cutoff} should be chosen to be about 30 Ryd and $d = 20 \text{ \AA}$. We thus have to work with the matrix $H_{\mathbf{k}}$ with $N_{\text{size}} = 1863$. Using the 2D approach, if we choose $2z_0 = d = 20 \text{ \AA}$, $\delta = 0.4 \text{ \AA}$ and $E_{\text{cutoff}} = 30$ Ryd, we have $N_z = 51$, $N_g = 39$ and thus $N_{\text{size}} = 1989$, close to that in the 3D approach. Though the obtained band structure of monolayer graphene is good, compared to that of the 3D approach, the resolution of wave functions in the real space is coarse. By decreasing δ , for instance, $\delta = 0.2 \text{ \AA}$ then $N_z = 101$ and $N_{\text{size}} = 3939$ we obtained good results of both the band structure and the wave function resolution. The matrix size in this case is larger than that in the 3D approach but the calculation is still faster. Even when we decreased δ to 1 \AA then $N_z = 201$ and $N_{\text{size}} = 7839$, the computational cost is still less expensive than that of the 3D approach because of the block tridiagonal structure of $H_{\mathbf{k}}$ in the 2D approach. In fact, using the 2D approach we did not need a large range of z . The data presented in this article were obtained from the choice of $z_0 = 10 \text{ \AA}$, $\delta = 0.1 \text{ \AA}$ and $E_{\text{cutoff}} = 30$ Ryd.

In Figure 2 we present the calculation results for the electronic structure of monolayer graphene obtained by the 3D and 2D approaches. The plots are superimposed for the aim of comparison. The data obtained by the 3D and 2D approaches are plotted in the dashed blue lines and in solid red lines, respectively. Our results are in very good agreement with those obtained by Fischetti *et al.* using the traditional 3D approach.¹⁸ From the figure we clearly observe the consistency of the two results in a large range of energy, from -40 eV upto 0 eV, i.e., covering the whole valence band and the most important part of the conduction band. In the higher energy range, however, the data obtained by the two approaches are not identical, except some typical curves which correspond to the π^* and σ^* bands. Such difference is easily understood since it originates from the limitation of the numerical description of unbound states whose energy dispersion curves in the conduction band usually take the typical parabolic form. For such states, the use of either the periodic or Neumann boundary conditions is always not relevant. For the π^* and σ^* bands, though lying in the very high energy range the corresponding wave functions are actually confined around the graphene layers, thus less sensitive to the boundary conditions. It thus explains why both calculation approaches result in almost identical dispersion curves. In Figure 3 we show the probability density distribution of finding electron in the space, $P_{n\mathbf{k}}(\mathbf{r}, z) = |\psi_{n\mathbf{k}}(\mathbf{r}, z)|^2$, in which the vector \mathbf{k} is chosen to point to the K -point $\mathbf{K} = (4\pi/3a_0, 0, 0)$, one of the six corner points of the hexagonal Brillouin zone, where $a_0 = 0.246 \text{ \AA}$ is the graphene lattice constant. We clearly observe the localisation behaviour of the states in a narrow two-dimensional space domain close to the material surfaces. Specifically, the states with $n = 1, 2$ and 3 show the concentration of their probability density at the position of the middle points connecting two nearest carbon atoms. These states belong to the σ band and are obviously responsible for the formation of the σ -bonds. For the states with $n = 4, 5$, belonging to the π -bands, we however see the concentration of their probability density at the two sides of the graphene lattice, close to the material surfaces, and in the middle regions of the two nearest carbon atoms. Such behaviours obviously reflect the nature of the π -bonds, formed by the hybridisation of the p_z orbitals. To see how the 3D and 2D approaches describing the decay of wave functions from the material layer surfaces we extracted data obtained by the two calculation approaches to check the variation of the probability density $P_{n\mathbf{k}}$ along the z -direction. In Figure 4 we show the variation of $P_{n\mathbf{K}}(z)$ for five states with $n = 1, 2, 3, 4, 5$. The blue solid curves present the data obtained by the 3D approach, and the red dashed curves for the 2D approach. In the linear scale plot we see the coincidence of the data obtained by the two calculation approaches (see the top panel of Figure 4). However, in the logarithmic scale (see the bottom panel of Figure 4) we see the difference between the two data sets: while the 2D approach clearly shows the decay of the

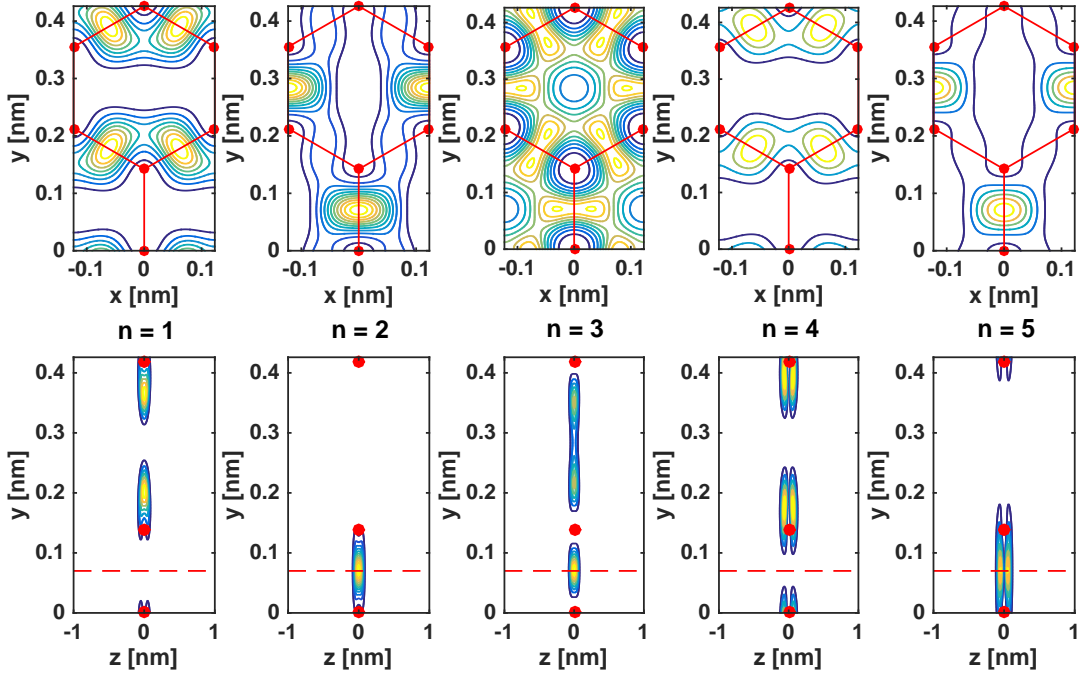


FIG. 3. Distribution of the probability density $P_{n\mathbf{k}}(x, y, z)$ of five lowest energy eigen-states ($n = 1, 2, 3, 4, 5$, see Figure 2) with the \mathbf{k} -vector taken at the K point $\mathbf{K} = (4\pi/3a_0, 0, 0)$, one corner point of hexagonal Brillouin zone. Five top sub-figures are the contour presentation of $P_{n\mathbf{k}}(x, y, z = 0)$ in the graphene lattice plane $z = 0$; the red solid circles and lines represent the carbon atoms lattice. Five bottom sub-figures are the contour presentation of $P_{n\mathbf{k}}(x = 0, y, z)$ taken in the plane $x = 0$ to show the concentration of the probability densities in the lattice plane and nearby the lattice surfaces. The red solid circles denote the carbon atoms and the red dashed line denotes the position at which the probability density $P_{n\mathbf{k}}$ is extracted and plotted in Figure 4.

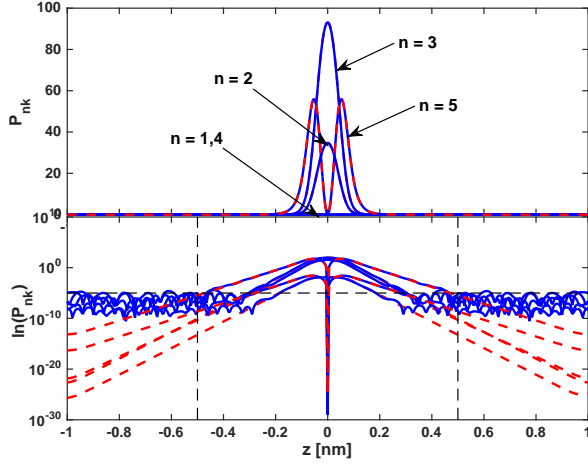


FIG. 4. Variation of the probability density $P_{n\mathbf{k}}$ ($n = 1, 2, 3, 4, 5$) along the red dashed lines denoted in Figure 3, i.e., the line going through the middle point connecting two nearest carbon atoms. The top and bottom panels show the results of $P_{n\mathbf{k}}(z)$ calculated by the 3D (denoted by the blue curves) and 2D (the red dashed curves) approaches in the linear and logarithmic scales, respectively. The horizontal and vertical black dashed lines in the bottom panel denote the accuracy order and trustworthy range of the probability densities calculated by the 3D approach.

bonding/anti-bonding wave functions in the natural exponent form $P_{n\mathbf{k}}(z) \propto e^{-\gamma|z|}$ in almost the whole range of z , the 3D approach only allows the description with the accuracy order of 10^{-5} when the inter-replica distance is chosen to be larger than 10 \AA .

The penetration of the electron wave functions into the space from the material surface is the origin of the interaction between the material layer and adjacent others. To see such effects it is interesting to consider the case of bilayer graphene, composed by **two** mono layer graphene stacked together. For simplicity we consider here only two typical stacking patterns, namely the AB- (Bernal) and AA-stacked configurations. In Figure 5 we show the electronic energy band structure of bilayer graphene, **Fig. 5(a)** and **5(b)** for the AA- and AB-stacked configurations, respectively. Differently from the case of monolayer graphene shown above, the 3D and 2D calculation approaches do not result in the perfect coincidence of the valance band of bilayer graphene (see the highest positions of the valance band at the Γ -point, for instance). This may result from the efficiency of the two approaches in describing the variation of wave functions along the z -direction as described in the previous paragraph. The electronic structure of monolayer and bilayer graphene are commonly shown in literature using the approaches of the tight-binding model and *ab initio* density functional

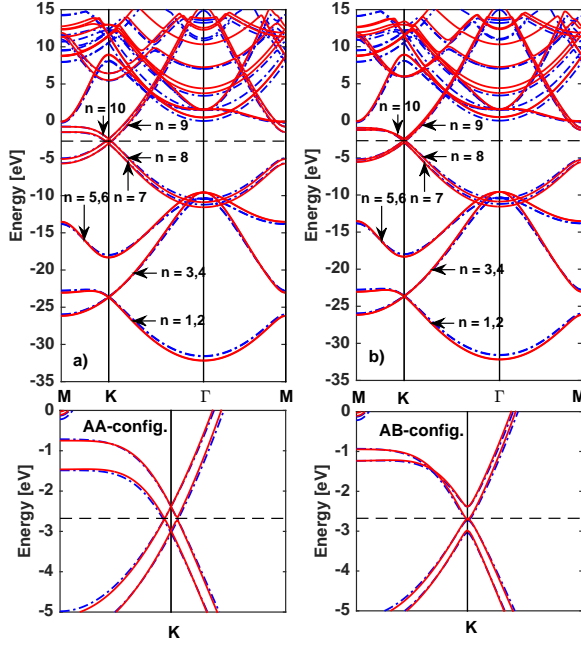


FIG. 5. Electronic band structure of bilayer graphene in the AA- (a) and AB-stacked (b) configurations calculated using two approaches: the blue dot-dashed lines are resulted from the 3D approach, and the red solid lines are from the 2D approach. The two small bottom subplots show the dispersion curves of low-energy excited states around the Dirac point. The horizontal black dashed lines denotes the Fermi energy level which is not yet shifted to 0 as usual. The labels $n = 1, 2, \dots, 10$ denote the energy bands.

theory.^{20,25} However, the demonstration usually focuses on the π bands in the energy range containing the Fermi energy level, and a rigorous comparison of the electronic structure of the mono-layer and bilayer graphene systems in the whole energy spectrum is lacking. On the basis of the Kurokawa empirical pseudopotential integrated in our 3D and 2D calculation codes we checked that the σ - and σ^* -bands of bilayer graphene are doubly degenerate and interestingly, they are identical to those of monolayer graphene. Nevertheless, for the π - and π^* -bands, the degeneracy is lifted and the electronic structures of the two bilayer configurations around the K -points show a qualitative difference, as observed in the two small subplots in Fig. 5. For the AA-stacked bilayer graphene, the π -bands are simply seen as the overlap of the π -bands of two monolayer graphene sheets but they are shifted from each other by a certain amount of energy. Different from that, the π -bands of the AB-stacked bilayer graphene shows the double-parabolic structure as seen in a small plot in Fig. 5. Such behaviours are in agreement with those predicted by the tight-binding and density functional theory calculations.^{19–25} The difference of the π -bands around the Dirac points in the AA- and AB-stacked configurations can be clearly understood using a model of empirical tight-binding for the p_z orbitals. Accordingly, the

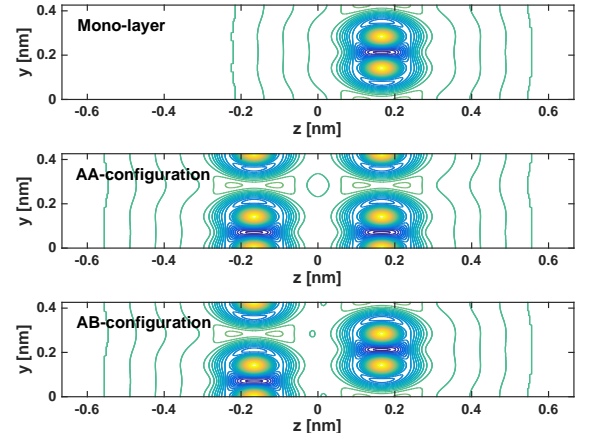


FIG. 6. Contour plot of the potential $V(x, y, z)$ in the real lattice space of the mono-layer (top panel), AA- (middle panel) and AB- (bottom panel) configurations. The plots are traced out on the plane $x = 0$.

origin of the difference is in the unequal dominance of the hybridisation of carbon atoms in the two sub-lattices in one material layer to those in the other layer.²⁶ Based on our approach, in what follows we will show additional data to highlight the origin of that difference.

First of all, let's look at the profile of the atomic potential in the real space of the two bilayer graphene lattices under consideration. In Figure 6 we show the variation of $V(x, y, z)$ calculated as the Fourier transform of the potential $V(\mathbf{g}, z)$ given by Eq. (9). The 2D contour plot is traced out on the plane $x = 0$, which contains four carbon atoms in the unit cell of the bilayer system. From the figure we clearly realise that the presence of the second atomic lattice almost does not cause any change in the potential value in the space domain close to the surfaces of the first layer, and vice versa, but it does in the narrow middle space between the two layers. This suggests that electrons occupying states whose probability density distribution concentrates at the position of the graphene lattice is not affected by the presence of the second layer. It thus explains the preservation of the σ -bands of mono-layer graphene in the electronic structure of the bilayer systems. However, electrons occupying the p_z orbitals will feel the presence of the second material layer since the corresponding probability density distribution is broadening on the space domains outside the material surfaces. The picture of the potential $V(\mathbf{g}, z)$ also supports this fact. Indeed, we see that the element $V(\mathbf{g}, z)$ with $\mathbf{g} = 0$ is present in all diagonal elements of the Hamiltonian matrix $H_{\mathbf{k}}$ and its value is dominant over all others with $\mathbf{g} \neq 0$. Additionally, the variation of $V(0, z)$ shows two deep wells centered at the position of the two graphene layers $z = \pm w/2$. It thus implies that the states belonging to the σ -band whose energy range is from -32 eV to -10 eV should be localised in the space domain defined by these quantum wells. In Figure 7 we show data supporting such conclusions through

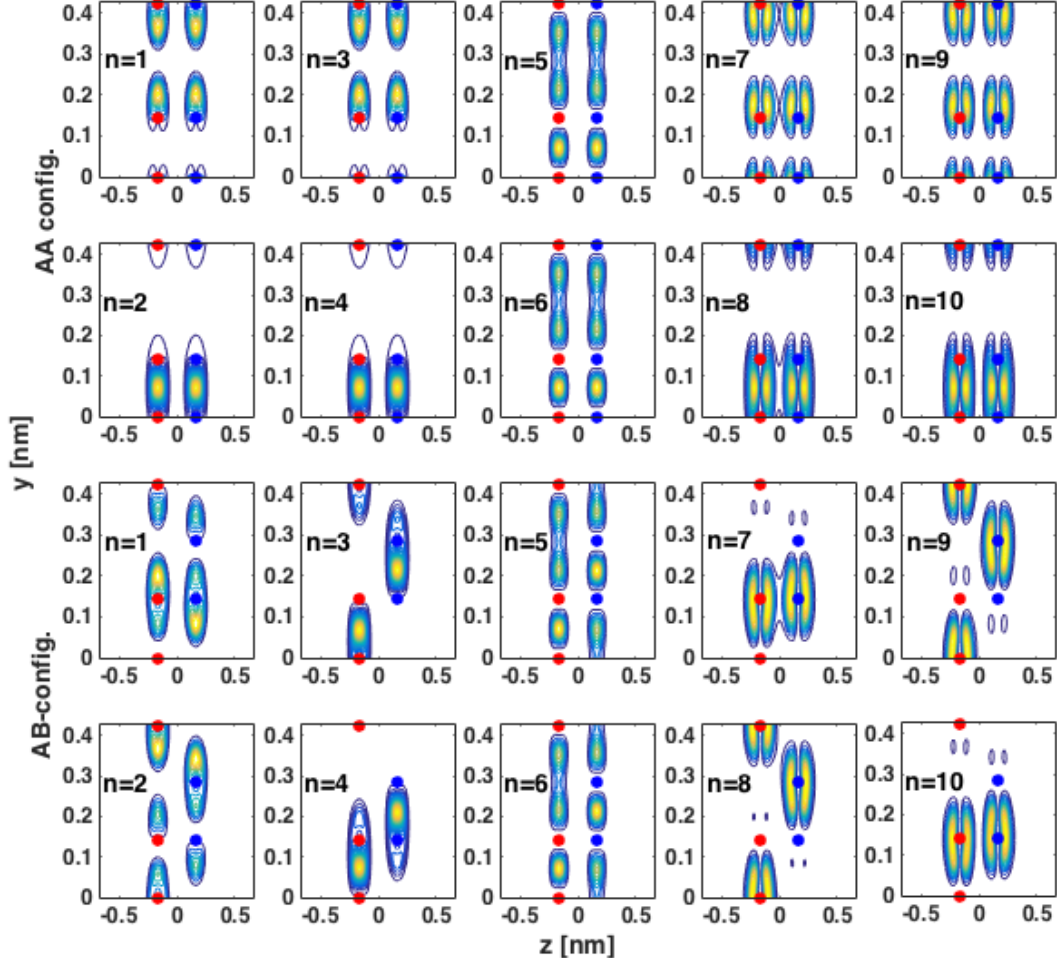


FIG. 7. Distribution of the probability densities $P_{n\mathbf{K}}(x, y, z)$ corresponding to ten eigenfunctions ($n = 1, 2, \dots, 10$) with the \mathbf{k} -vector determined at the K-point of the AA- (ten upper subplots) and AB-stacked (ten lower subplots) graphene configurations. The red and blue solid circles denote the position of carbon atoms in each graphene layer. The plots are restricted for y in the primitive cell, $0 \leq y < \sqrt{3}a_0$ where a_0 is the primitive vector length (chosen as unit). The data are traced out on the plane $x = 0$.

the picture of the distribution of the probability density for ten eigenstates in the valence band at the K-point, $P_{n\mathbf{K}}(\mathbf{r}, z) = |\psi_{n\mathbf{K}}(\mathbf{r}, z)|^2$, $n = 1, 2, \dots, 10$. The 2D plots are traced out on the plane $x = 0$ which contains four carbon atoms in the unit cell. We clearly see the strong localisation of the wave functions (corresponding to $n = 1, 2, \dots, 6$) with the centres located at the position of the graphene layers, $z = \pm w/2$, as expected; their broadening at $z = 0$ (the centre plane between the two graphene layers) is very small $P_{n\mathbf{K}}(\mathbf{r}, z = 0) \# 10^{-4}$. For the states with $n = 7, 8, 9$ and 10 whose energies are close to the wellhead, therefore their formation is also governed by the other potential terms $V(\mathbf{g}, z)$ with $\mathbf{g} \neq 0$. It should be noticed from Figure 1 that the variation of $V(\mathbf{g}, z)$ versus z always shows a symmetric behaviour for all \mathbf{g} and $V(\mathbf{g}, z)$ is real in the AA-stacked configuration. In contrast, in the AB-configuration, $V(\mathbf{g}, z)$ shows an asymmetric behaviour and takes a complex value for some reciprocal lattice vectors \mathbf{g} . It thus explains the

difference in the electronic structure of the two bilayer graphene configurations around the Dirac point. With the behaviour shown in Figure 7 the wave functions (with $n = 7, 8, 9, 10$) can be interpreted as the result of the hybridisation of the p_z orbitals in two graphene layers and represent the coupling between the two layers. Subplots with $n = 7$ and 8 show clearly the emergence of the hybridisation.

Last but not least, to shed light into the coupling between the two graphene layers we calculated the electron density $\rho(x, y, z)$ in the bilayer graphene systems and then subtracted it to the summation of the electron density $\rho_{1,2}$ of two independent graphene layers put at the positions $z = \pm w/2$. The quantity $\delta\rho = \rho - (\rho_1 + \rho_2)$ provides the information of the polarisation of spatial charge density formed by the coupling between the two graphene layers. The obtained results are shown in Figure 8 for the AA- (two top panels) and AB- (two bottom panels) configurations. The 2D contour plots are also

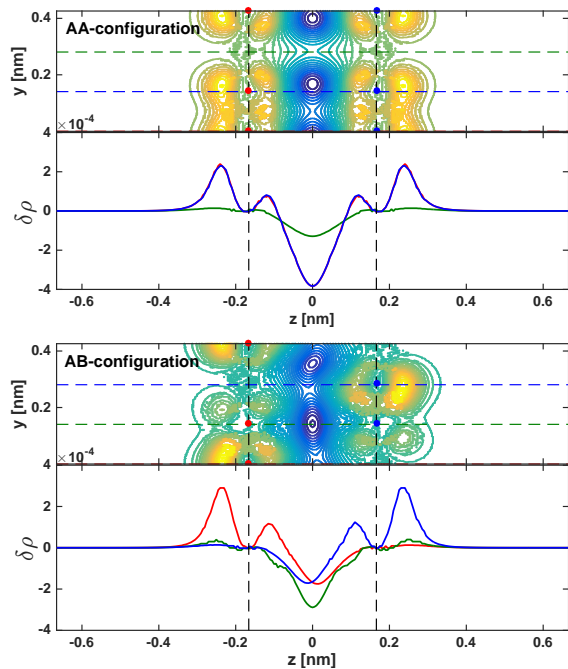


FIG. 8. Distribution of spatial charge density $\delta\rho = \rho - (\rho_1 + \rho_2)$ calculated as the difference of the charge density of bilayer graphene ρ from the summation of those of the **two** independent mono-layer graphene $\rho_{1/2}$ located at the position of layers 1 and 2 ($z = \pm w/2$). The contour plots are traced out on the plane $x = 0$. The line plots are traced out along the dashed lines denoted in the contour plots.

traced out on the plane $x = 0$. The 1D plots show the variation of $\delta\rho$ versus z along the dashed lines denoted in the contour plots. As expected, the value of $\delta\rho$ in the bilayer graphene configurations is not equal to zero in the whole range of z , but it shows the picture of different structures depending on the detail of atomic configurations. Additionally, the profile of $\delta\rho$ always shows the dominant characteristics of the hybridised p_z states with two significant peaks located at two sides, close to the surfaces, of each graphene layer. The dip of ρ located at $z = 0$ apparently plays the role of keeping the two

graphene layers in attraction with each other. So, associated with the potential picture shown in Figure 6, we can conclude that the two graphene layers always couple with each other; the interaction between the two layers causes the polarisation of the spatial charge density contributed by electrons occupying the hybridised p_z states which, consistently, play the essential role for the attraction between two graphene layers.

IV. CONCLUSION

To conclude, we have proposed a calculation approach for the electronic structure of two-dimensional materials to avoid the construction of artificial bulk systems. The method is the combination of the plane wave method and the real-space treatment based on the finite differential method to represent the periodic variation in the material plane and the decay of electron wave functions from the material surfaces. We formulated the secular equation for the electronic structure and showed that the proposed approach leads to working with matrices whose structure is tridiagonal in blocks, instead of matrices with the full structure as in the three-dimensional approach. Associated with the empirical pseudopotential method we used the Kurokawa potential to revisit some fundamental issues of bilayer graphene. We supplementally show some evidences, from the first-principles viewpoint, such as the potential profile in the lattice space, the electron density and the polarisation of spatial charge density, to explain the coupling between two graphene layers, why the σ -bands of monolayer graphene are preserved in the electronic structure of bilayer graphene, and why the difference in the electronic structure of the AA- and AB-stacking configurations around the Dirac point. Our calculation approach and analysis as presented may be suitable for investigating different aspects of the so-called van der Waals 2D hetero-structures, which have been recently attracting an intense consideration.

The authors are grateful to Philippe Dollfus for fruitful discussions. This work was supported by Hanoi University of Science and Technology under the project No. T2016-LN-02.

* To whom correspondence Email to: van-nam.do@gmail.com

¹ K. S. Novoselov, A. K. Geim, S. V. Morozov, D. Jiang, Y. Zhang, S. V. Dubonos, I. V. Grigorieva and A. A. Firsov, *Electric field effect in atomically thin carbon films*, Science **306**, 666 (2004).

² A. K. Geim and I. V. Grigorieva, *Van der Waals heterostructures*, Nature **499**, 419 (2013).

³ Y. Liu, N. O. Weiss, X. Duan, H. C. Cheng, Y. Huang and X. Duan, *Van der Waals heterostructures and devices*, Nat. Rev. Mats. **1**, 16042 (2016).

⁴ P. Cudazzo, I. V. Tokatly and A. Rubio, *Dielectric screen-*

ing in two-dimensional insulators: implications for exciting and impurity states in graphene, Phys. Rev. B **84**, 085406 (2011).

⁵ V. M. Silkin, J. Zhao, F. Guinea, E. V. Chulkov, P. M. Echenique and H. Petek, *Image potential states in graphene*, Phys. Rev. B **80**, 121408 (2009).

⁶ S. Latini, T. Olsen and K. S. Thygesen, *Excitons in van der Waals heterostructures: the important role of dielectric screening*, Phys. Rev. B **92**, 245123 (2015).

⁷ V. U. Nazarov, *Electronic excitations in quasi-2D crystals: what theoretical quantities are relevant to experiment?* New J. Phys. **17**, 073018 (2015).

- ⁸ C. A. Rozzi, D. Varsano, A. Marini, E. K. U. Gross and A. Rubio, *Exact Coulomb cutoff technique for supercell calculation*, Phys. Rev. B **73**, 205119 (2006).
- ⁹ A. Castro, E. Rasanen and C. A. Rozzi, *Exact Coulomb cutoff technique for supercell calculations in two dimensions*, Phys. Rev. B **80**, 033102 (2009).
- ¹⁰ L. H. Ye, *Surface calculations with asymmetrically long-ranged potentials in the full-potential linearised augmented plane-wave methods*, Phys. Rev. B **92**, 115132 (2015).
- ¹¹ J. Enkovaara *et al.*, *Electronic structure calculations with GPAW: a real-space implementation of the projector augmented wave method*, J. Phys.: condens. matter **22**, 253202 (2010).
- ¹² E. P. Trevisanutto and G. Vignale, *Ab-initio electronic structure of quasi-two-dimensional materials: a native Gaussian-plane wave approach*, J. Chem. Phys. **144**, 204122 (2016).
- ¹³ I. Y. Zhang, X. Ren, P. Rinke, V. Blum, and M. Scheffler, *Numeric atom-centered-orbital basis sets with valence-correlation consistency from H to Ar*, New J. Phys. **15**, 123033 (2013).
- ¹⁴ E. Polizzi, *Density-matrix-based algorithm for solving eigenvalue*, Phys. Rev. B **79**, 115112 (2009); <https://software.intel.com/en-us/node/470372>
- ¹⁵ V. N. Do, *Non-equilibrium Green function method: theory and application in simulation of nanometer electronic devices*, Adv. Nat. Sci.: Nanosci. and Nanotechnol. **5** 033001 (2014).
- ¹⁶ A. Molina-Sanchez, A. Garcia-Cristobal and G. Bester, *Semiempirical pseudopotential approach for nitride-based nanostructures and ab initio based passivation of free surfaces*, Phys. Rev. B **86**, 205430 (2012).
- ¹⁷ Y. Kurokawa, S. Nomura, T. Takemori and Y. Aoyagi, *Large-scale calculation of optical dielectric functions of diamond nanocrystallites*, Phys. Rev. B **61**, 12616 (2000).
- ¹⁸ M. V. Fischetti, J. Kim, S. Narayanan, Z.-Y. Ong, C. Sachs, D. K. Ferry and S. J. Aboud, *Pseudopotential-based studies of electron transport in graphene and graphene nanoribbons*, J. Phys.: Condens. Matter **25**, 043202 (2013).
- ¹⁹ E. McCann, *Asymmetry gap in the electronic band structure of bilayer graphene*, Phys. Rev. B **74**, 161403 (2006).
- ²⁰ E. McCann, D. S. L. Abergel and V. I. Fal'ko, *The low energy electronic band structure of bilayer graphene*, Eur. Phys. J. **148**, 91 (2007).
- ²¹ Y. Zhang, T. T. tang, C. Girit, Z. Hao, M. C. Martin, A. Zettl, M. F. Crommie, Y. R. Shen and F. Wang, *Direct observation of widely tunable bandgap in bilayer graphene*, Nature **459**, 820 (2009).
- ²² J. B. Oostinga, H. B. Heersche, X. Liu, A. F. Morpurgo, and L. M. K. Vandersypen, Nat. Mater. **7**, 151 (2007).
- ²³ S. Latil, V. Meunier and L. Henrard, *Massless fermions in multilayer graphitic systems with misoriented layers: ab initio calculations and experimental fingerprints*, Phys. Rev. B **76**, 201402 (2007).
- ²⁴ E. V. Castro, K. S. Novoselov, S. V. Morozov, N. M. R. Peres, J. M. B. Lopes dos Santos, J. Nilsson, F. Guinea, A. K. Geim and A. H. Castro Neto, Phys. Rev. Lett. **99**, 216802 (2007).
- ²⁵ E. McCann and M. Koshino, *The electronic properties of bilayer graphene*, Rep. Prog. Phys. **76**, 056503 (2013).
- ²⁶ A. V. Rozhkov, A. O. Sboychakov, A. L. Rakhmanov and F. Nori, *Electronic properties of graphene-based bilayer systems*, Phys. Rep. **648**, 1 (2016).